Promising Potential of Nanostructured $DyFeO_3$ Photocatalyst for Environmental Remediation: Authenticity and Stability

Mohasin Tarek, Ferdous Yasmeen, and M. A. Basith*

Nanotechnology Research Laboratory, Department of Physics, Bangladesh University of Engineering and Technology, Dhaka-1000, Bangladesh.

E-mail: mabasith@phy.buet.ac.bd

Abstract

Understanding the authentic nature and stability of a photocatalyst through diverse experiments and calculations is crucial for advancing environmental remediation. In this study, we synthesized nano-sized $DyFeO_3$ particles with a porous structure, featuring an average pore size of 40 nm, to meticulously evaluate their photocatalytic efficacy in degrading aquatic pollutants under solar irradiation. These nanoparticles exhibit a direct band gap of 2.1 eV, rendering them well-suited for effective solar light absorption. Additionally, the conduction band minimum (CBM) suggests potential participation in reduction reactions, while the valence band maximum (VBM) is conducive to oxidation reactions. To confirm the authentic catalytic efficiency of $DyFeO_3$ photocatalysts, we assessed their ability to degrade both colored Rhodamine B (RhB) and colorless antibiotic Levofloxacin (LFX). Notably, their photocatalytic performance in decomposing the colorless pollutant LFX, alongside the colored RhB, eliminates any potential influence of dye sensitization. Moreover, the presence of $DyFeO_3$ in the solution medium decreased the activation energy of LFX degradation from 38.4 kJ mol^{-1}

K^{-1} to 34.1 kJ mol^{-1} K^{-1} , providing further evidence of their true catalytic function. Furthermore, their apparent Quantum Yield (AQY) values of 28.94% and 32.83% for RhB and LFX degradation, respectively, demonstrate superior solar energy harvesting capability compared to commercially available TiO_2. The high degradation efficiency, high quantum yield, and excellent stability of single-structured $DyFeO_3$ nanoparticles indicate their considerable potential for large-scale production in photocatalytic and related applications.

Introduction

The sustenance of human existence heavily relies on abundant access to uncontaminated water. However, over time, clean water resources are depleting rapidly.[1,2] Addressing this pressing challenge necessitates developing an efficient, environmentally friendly, and sustainable system. In this context, photocatalysis emerges as a promising solution.[3–5] Photocatalysts capable of purifying water through this process utilize light energy to generate electron-hole pairs, initiating redox reactions at their surface.[3,5,6] This mechanism enables the degradation of water pollutants. Utilizing sunlight as the primary light source is particularly advantageous due to its abundance and cleanliness.[6] With an annual irradiation of 3.85 yotta joules (YJ) of energy on Earth's surface, sunlight stands as an unparalleled renewable resource.[7] Therefore, harnessing photocatalysts to degrade pollutants under sunlight exposure represents a sustainable and environmentally conscious method of water purification.

The performances and reliability of photocatalysis relies significantly on the right choice of catalyst.[5,8] A sustainable and reliable photocatalyst for solar light-driven photocatalytic wastewater treatment must possess several essential characteristics to ensure efficient performance. It should exhibit high photocatalytic activity, efficiently converting solar energy (UV and visible portion) into chemical energy for pollutant degradation.[9–11] Stability and durability of the catalysts in aqueous or other environments are paramount, ensuring long-term performance without degradation or deactivation.[12] Selectivity towards target

pollutants, along with the minimal generation of harmful byproducts, is crucial to prevent secondary environmental concerns.[12] Finally, the ease of synthesis and integration streamlines the implementation into existing wastewater treatment infrastructure or novel systems, thus facilitating the transfer of technology from the laboratory to real-life applications. By encompassing these characteristics, the photocatalyst can effectively utilize solar energy to degrade pollutants in wastewater, contributing to sustainable and eco-friendly water treatment solutions. Conventional photocatalysts such as TiO_2,[13] ZnO,[14] and SnO_2 are widely utilized, with TiO_2 drawing particular interest due to its potential in solar light-driven photocatalysis.[13] However, its high optical bandgap of approximately 3.2 eV[15] results in inefficiencies, limiting its ability to utilize visible light, which constitutes a substantial portion of the solar spectrum.[13,16] This limitation severely restricts its effectiveness. Currently, various approaches, including doping,[17] nanocomposite formation,[18,19] molecular cross-linking,[20] intricate structural design,[21] and chemical modifications,[22] are employed to enhance light absorption. Nevertheless, these strategies often introduce complexity, reduce reliability, and increase costs.

Recently, orthoferrite-based perovskite oxides—designated as $AFeO_3$, with A representing elements like Ce,[23] Sr,[24] Bi,[25] Sm,[26] La,[27] Pr,[28] Gd,[29] among others—have garnered attention for their promising photocatalytic properties. These materials exhibit favorable characteristics such as an appropriate bandgap, stability, high surface area, presence of oxygen vacancies, porosity, and redox ability. Utilizing solar light, these orthoferrite-based perovskite oxides demonstrate successful photocatalytic wastewater treatment.[30] Among various perovskite oxide materials, $DyFeO_3$ has been extensively studied in spintronics applications owing to its excellent magnetic properties, including a high Bohr magnetron value.[31] However, despite possessing notable attributes such as a suitable band gap, oxygen vacancies, and diverse oxidation states, $DyFeO_3$ remains relatively unexplored as a promising candidate for applications beyond spintronics, especially in the fields of photocatalytic wastewater treatment.

In perovskite-structured materials like $DyFeO_3$, oxygen vacancies, as an inherent characteristic,[32] play a crucial role in boosting charge separation, surface reactivity, electronic properties, redox reactivity, and reducing recombination rates. Furthermore, the diverse oxidation states inherent in $DyFeO_3$ perovskite oxide may endow it with versatile redox properties, facilitating the oxidation and reduction reactions crucial for pollutant degradation.[33] Specifically, during photocatalytic processes, the varied oxidation states of dysprosium (Dy) and iron (Fe) ions could create efficient electron transfer pathways, thereby promoting the generation and transfer of reactive oxygen species (ROS) such as hydroxyl radicals ($\bullet OH^-$), superoxide radical ($\bullet O_2^-$). These ROS are crucial intermediates in the degradation of organic pollutants found in wastewater.

To accurately assess the photocatalytic performance of a catalyst using dyes under solar light irradiation, it is crucial to meticulously consider several precautions. This is due to the fact that numerous dyes possess the capability, upon photoexcitation, to introduce an electron into the conduction band of a semiconductor. This characteristic finds extensive application in dye-sensitized solar cells (DSSC), where dyes are combined with a photocatalyst typically comprising a semiconductor oxide. In this scenario, the dye absorbs radiation rather than the semiconductor oxide.[34] To ensure that the degradation is solely photocatalytic rather than dye-sensitized, it is necessary to evaluate the photocatalytic performance using a colorless probe such as ciprofloxacin. Secondly, evaluating the activation energy of pollutants is crucial for understanding the kinetic barriers involved in degradation reactions, aiding in the selection of appropriate catalysts and reaction conditions to enhance degradation efficiency. Thirdly, the catalyst must efficiently convert absorbed photons, particularly sunlight, into reactive species, indicating a high apparent quantum yield efficiency. A high apparent quantum yield signifies a more efficient utilization of light energy, leading to enhanced reaction rates and overall performance of the photocatalyst. In addition to careful considerations during the photocatalytic process, post-photocatalysis characterization involving structural, morphological, and chemical analyses is essential for evaluating

catalyst stability and enhancing performance. These measures aid in the development of more effective and sustainable photocatalytic systems. However, it is noteworthy that such experiments and precautions have been insufficiently explored in numerous prior studies on photocatalytic water treatment.

Therefore, in this investigation, we aimed to validate the genuine photocatalytic efficacy of the $DyFeO_3$ photocatalyst. We achieved this by observing the degradation of both colored (Rhodamine B) and colorless (levofloxacin) pollutants, determining the activation energy of RhB and LFX pollutants, quantifying the apparent quantum yield efficiency of the $DyFeO_3$ photocatalyst, and examining the stability and reusability of $DyFeO_3$ photocatalysts through post-photocatalysis characterization using various techniques such as XRD and XPS. Furthermore, to ascertain the practical utility of $DyFeO_3$ nanoparticles, their efficiency in degrading LFX is compared with that of commercially available TiO_2, a widely used photocatalyst.

Materials preparation and experimental techniques

Materials

In this investigation, the following analytical grade reagents were used for materials synthesis: $Dy(NO_3)_3{\cdot}5H_2O$ (Sigma-Aldrich, 99.80%), $Fe(NO_3)_3{\cdot}9H_2O$ (Sigma-Aldrich, 98.00%), citric acid ($C_6H_8O_7$), NH_4OH, ethylene Glycol CH_2OHCH_2OH, Rhodamine B (RhB), levofloxacin (LFX), titanium oxide (TiO_2), isopropanol (IPA), acrylamide, $K_2Cr_2O_7$, and EDTA – 2Na. All chemicals were purchased from Sigma-Aldrich, Germany. These compounds were utilized without undergoing any further purification.

Synthesis method characterization

$DyFeO_3$ perovskite nanoparticles were synthesized using a sol-gel technique as shown in Fig. S1. Synthesis and characterization techniques are described in detail in our recent article.[35]

Photocatalytic characterization

Schematically a photocatalytic reactor setup for the pollutant degradation experiments was shown in Fig. S2. The degradation process commenced with the dissolution of 1.2 mg of Rhodamine B (RhB) in 100 ml of distilled water, followed by the measurement of its absorbance spectrum through a UV-vis spectrophotometer (UV-2600, Shimadzu, Japan). Subsequently, 40 mg of $DyFeO_3$ nanoparticles photocatalyst was introduced into 50 ml of the RhB solution, and the mixture was stirred in the dark for an hour to establish an adsorption-desorption equilibrium between the photocatalyst and RhB. The photocatalytic reaction was initiated by exposing the solution to a 500 W Hg-Xn lamp with an irradiance of 100 mW cm^{-2} in the solar spectrum. After 30 minutes of illumination, 4 ml of the suspension was extracted and centrifuged at 6500 rpm for 2 minutes. The absorbance spectrum of the resulting mixture was then measured to determine the concentration of the remaining RhB. This cyclic process was repeated over 4 hours at 30-minute intervals.

For Levofloxacin (LFX) degradation, a solution was prepared by dissolving 1 mg of LFX in 100 ml of distilled water. Subsequently, 20 mg of $DyFeO_3$ nanoparticles photocatalyst was added to 50 ml of the LFX solution, and the ensuing procedures mirrored those described for RhB degradation.

Active species trapping experiments were conducted under solar illumination, incorporating four distinct scavengers: hydroxyl ($\bullet OH^-$), superoxide radical ($\bullet O_2^-$), electrons (e^-), and holes (h^+). The impact on degradation efficiency was assessed by introducing 1.5 mM of isopropanol (IPA), acrylamide, $K_2Cr_2O_7$, and EDTA – 2Na as quenchers for $\bullet$OH-, $\bullet O_2^-$, e^-, and h^+, respectively.

In the determination of activation energy experiment, a 1 mg LFX solution was created in 100 ml distilled water, with 10 mg of $DyFeO_3$ nanoparticles added to 25 ml of the LFX solution. After stirring in the dark for an hour, achieving an adsorption-desorption equilibrium, the solution was exposed to a solar simulator. The absorbance spectrum was measured after 30 minutes of illumination at different temperatures. Additionally, the process was repeated

without the addition of $DyFeO_3$ nanoparticles to the LFX solution.

Results and discussion

Structural, morphological and chemical state analysis

In our recent publication,[35] the powder X-ray diffraction (XRD) analysis of $DyFeO_3$ unveiled an orthorhombic crystal structure within the *pnma* space group,[36] indicating its nanoparticle formation with a crystallite size of approximately 48.72 nm.

Furthermore, examination of the surface morphology through field emission scanning electron microscopy (FESEM) and transmission electron microscopy (TEM) confirmed the successful formation of nano-sized $DyFeO_3$ particles characterized by a porous structure, with an estimated pore size of approximately 40 nm. X-ray photoelectron spectroscopy (XPS) analysis of the $DyFeO_3$ nanoparticles revealed the presence of Dy^{4+}, Dy^{3+}, Fe^{2+}, Fe^{3+}, and O^{2-} ions, which contribute to increased redox activity, facilitating enhanced pollutant degradation.[37–40] Notably, deconvolution of the high-resolution O-1s XPS spectra exhibited two distinct peaks at 529.53 and 531 eV, corresponding to metal-oxygen bonds and oxygen vacancies, respectively, with molar ratios of 61.33% and 38.67%.[40] Oxygen vacancies, stemming from missing oxygen atoms in the lattice, are induced by the mixed oxidation states of transition metal ions (Fe^{2+} and Fe^{3+}) and rare earth ions (Dy^{3+} and Dy^{4+}), contributing to improved charge carrier generation and transfer.[32] This phenomenon augments the photocatalytic activity of $DyFeO_3$, holding significant promise for various applications.

In the synthesis of $DyFeO_3$ nanoparticles via the sol-gel method utilizing ethylene glycol as a chelating agent results in the formation of a porous structure due to the thermal decomposition of ethylene glycol, which creates internal pressure leading to void formation, while calcination at 750°C and controlled N_2 atmosphere further enhances pore formation and oxygen vacancy generation, crucial for the porous structure of $DyFeO_3$.[41–43] Notably, these structural features may collectively enhance the catalytic performances of $DyFeO_3$

nanoparticles.

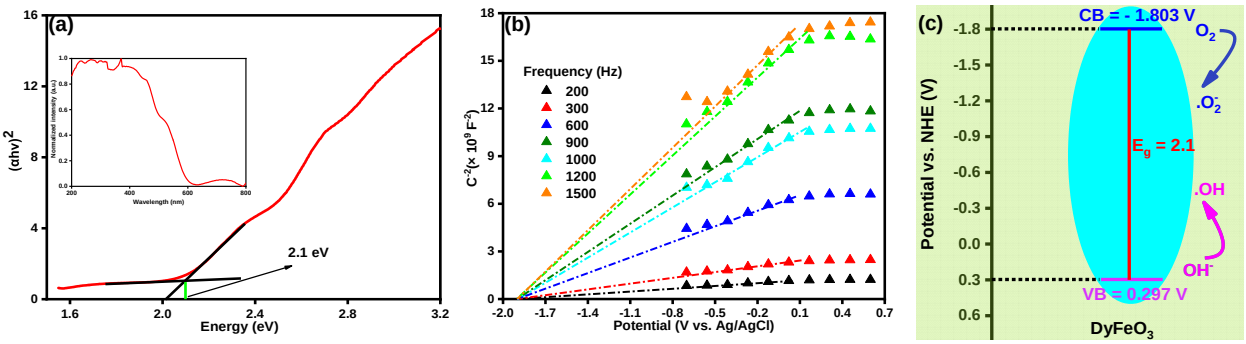

Figure 1: **The optical properties and band edge characteristics of $DyFeO_3$ nanoparticles were investigated for their potential applications in solar-driven degradation of organic pollutants in wastewater.** The Tauc plot **(a)** reveals a direct band gap of 2.1 eV, rendering the nanoparticles suitable for efficient solar light absorption. The inset in (a) displays normalized optical absorption spectra, with distinct peaks at different wavelengths indicating variations in the oxidation states of elements within $DyFeO_3$ nanoparticles. Mott–Schottky plots **(b)** at different frequencies affirm the n-type semiconductor behavior of $DyFeO_3$, establishing a flat band potential of -1.90 V with respect to an Ag/AgCl electrode. The electronic band structure schematic **(c)** illustrates a substantial conduction band minimum (CBM), indicating the potential for oxygen reduction reaction (ORR), and a positive CBM, suggesting suitability for oxidation reactions. These attributes collectively contribute to the nanoparticles' efficacy in pollutant degradation within wastewater treatment processes

Optical characterization

The optical properties and band edge characteristics of $DyFeO_3$ nanoparticles were examined to evaluate their potential for solar-driven degradation of organic pollutants in wastewater. These attributes were assessed using Tauc and Mott-Schottky methodologies, with the outcomes depicted in Fig. 1. The distinct absorption characteristics observed in the wavelength range of 200 nm to 590 nm, as illustrated in the inset of Fig. 1(a), signify the transition of photoexcited electrons from the valence band (VB) to the conduction band (CB), a characteristic behavior commonly associated with semiconductor materials. Note that the prominent peaks within that wavelength range correspond to the electron transition from the valence band to the conduction band of Dy, Fe, and O atoms. The direct band gap of 2.1 eV for $DyFeO_3$ nanoparticles was determined via a Tauc plot[44] analysis.

To experimentally obtain band edge positions, Mott–Schottky[45] analysis was carried out at various frequencies, and the results are depicted in Fig. 1(b). In Fig. 1(b), the quasi-linear behavior and the negative x-intercept value of −1.90 V vs. Ag/AgCl in the Mott-Schottky analysis for $DyFeO_3$ nanoparticles, irrespective of frequency (200-1500 Hz), suggests that $DyFeO_3$ is the n-type semiconductor.[46,47] This result implies that the majority of carriers in $DyFeO_3$ are electrons. Moreover, the frequency independence of the flat band potential could be attributed to a uniform carrier density and the relative absence of frequency-dependent phenomena, highlighting the robust electronic properties of $DyFeO_3$.

Utilizing the Mott-Schottky plot's x-intercept and the band gap information obtained from the Tauc plot, we determined the valence band maximum (VBM) and conduction band minimum (CBM) positions for $DyFeO_3$ as 0.297 V and −1.803 V vs. NHE, respectively, which is displayed in Fig. 1(c). The flat band potential (E_{fb}) is established at -1.90 V (as shown in Fig. 1(b)) for $DyFeO_3$ nanoparticles ∼ Ag/AgCl based on the Mott-Schottky formula.[48,49] This value is subsequently transformed to -1.703 V versus the normal hydrogen electrode (NHE) using the equation $E_{NHE} = E_{Ag/AgCl} + 0.197\,V$.[47,49] In the realm of n-type semiconductors, E_{fb} exhibits a close association with the conduction band (CB) and tends to be approximately 0.1 V more positive than its conduction band potentials (E_{CB}).[49] Consequently, the calculated E_{CB} for $DyFeO_3$ nanoparticles is roughly estimated to be -1.803 V (∼ NHE). The graphical representation in Fig. 1 visually supports these outcomes concerning E_g, E_{VB}, and E_{CB}, showcasing a coherent alignment with the expression: $E_{VB} = E_{CB} + E_g$.[49] The elevated CBM of −1.803 V indicates that $DyFeO_3$ nanoparticles have potential involvement in reduction reactions, notably the oxygen reduction reaction (ORR).[46] In the context of ORR, wherein oxygen (O_2) is reduced to superoxide (O_2^-) through electron acceptance, the standard redox potential for O_2/O_2^- is approximately 0.28 V vs. NHE. However, the positive VBM value implies the existence of hole states in $DyFeO_3$'s valence band, suggesting favorability for participating in oxidation reactions, such as OH^-/OH. This dual propensity of $DyFeO_3$ nanoparticles indicates the potential redox reaction, which may

greatly enhances the photocatalytic pollutant degradation process.

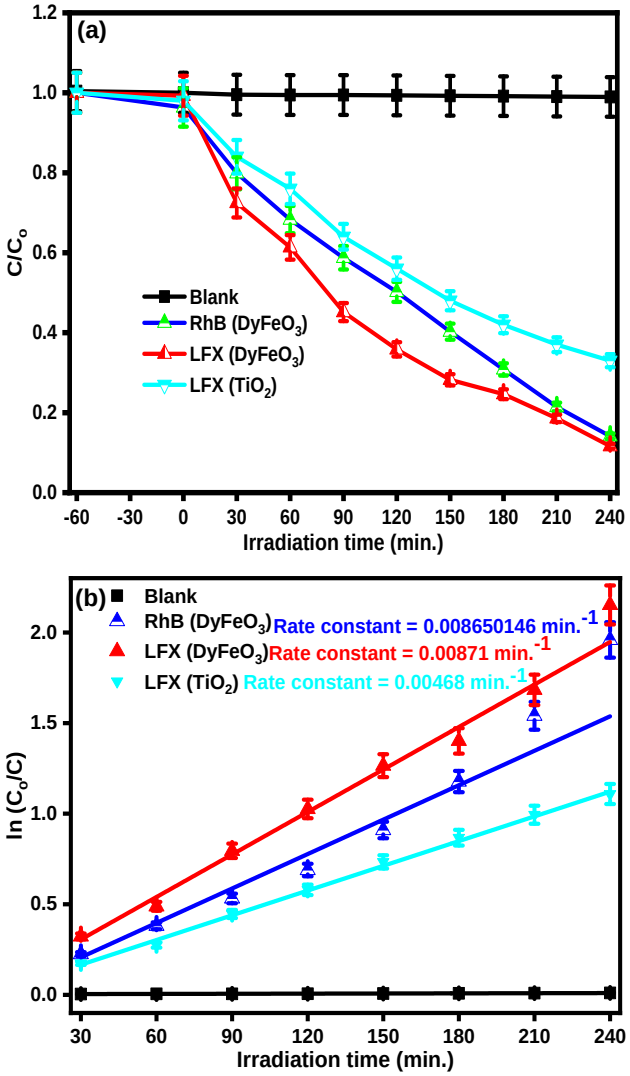

Figure 2: **The photocatalytic efficacy of $DyFeO_3$ nanoparticles was evaluated and compared to that of the commercially available TiO_2 photocatalyst**. **(a)** Under Hg-Xe lamp (500 W) illumination, $DyFeO_3$ nanoparticles demonstrated superior photocatalytic degradation of industrial dye (RhB) and pharmaceutical antibiotic (LFX) compared to TiO_2. **(b)** Pseudo-first-order kinetic fitting revealed a significantly faster degradation rate for RhB and LFX in the presence of $DyFeO_3$ nanoparticles compared to TiO_2 photocatalyst.

Photocatalytic performances evaluation

To assess the solar light-driven efficiency of synthesized $DyFeO_3$ nanoparticles for photocatalytic degradation, their performance was evaluated and compared with the industrially

prevalent TiO_2 photocatalyst under identical conditions. The corresponding experimental setup is schematically shown in Fig. S2. To authentically assess the photocatalytic impact of $DyFeO_3$ nanoparticles under simulated solar irradiation, we investigated the degradation rates of both a colored pollutant, Rhodamine B (RhB), and a colorless pollutant, levofloxacin (LFX). This approach allows us to discern the distinct photocatalytic responses influenced by the inability of colorless LFX to sensitize a photocatalytic reaction under solar illumination. Absorbance curves in Fig. S3(a,b) revealed a time-dependent reduction in peak intensity with a hypsochromic shift, indicating the degradation of RhB and LFX under the UV-vis spectrum with the presence of $DyFeO_3$ photocatalyst.[47] The photocatalytic efficiency of $DyFeO_3$ nanoparticles to degrade the industrial dye (RhB) and pharmaceutical antibiotic (LFX) is evaluated using the following equation:[19,50]

$$\text{Photocatalytic degradation } (\%) = \left(\frac{C_0 - C}{C_0}\right) \times 100 \tag{1}$$

Here, C_0 is the initial concentration of the pollutant, while C represents the concentration of the remaining pollutant at a particular time of irradiation. The C/C_0 time plot depicted in Fig. 2(a) reveals that $DyFeO_3$ exhibited significant degradation efficiencies, reaching 85.9% for RhB and 88.% for LFX., surpassing the performance of TiO_2, which exhibited a 67% degradation rate for LFX. This enhanced photocatalytic activity in $DyFeO_3$ can be attributed to its oxygen vacancies, porous structure, and favorable band edge positions.

Further kinetic analysis employing a pseudo-first-order kinetics model where the experimental data were subjected to a fitting approach utilizing a pseudo-first-order model based on the following equation:[19,50]

$$\ln\left(\frac{C_0}{C}\right) = kt \tag{2}$$

Here, k is the reaction rate constant, while t is the irradiation time. The value of k was calculated from the slope of $\ln(C_0/C)$ vs. t graph. The findings were illustrated in Fig. 2(b), which revealed markedly elevated rate constants (k) for the degradation of RhB and

LFX in the presence of the $DyFeO_3$ photocatalyst compared to the degradation of LFX with the TiO_2 photocatalyst. The superiority of our porous structure $DyFeO_3$ photocatalyst is demonstrated by comparing its performance with previously studied perovskite photocatalysts, as outlined in Table S1.

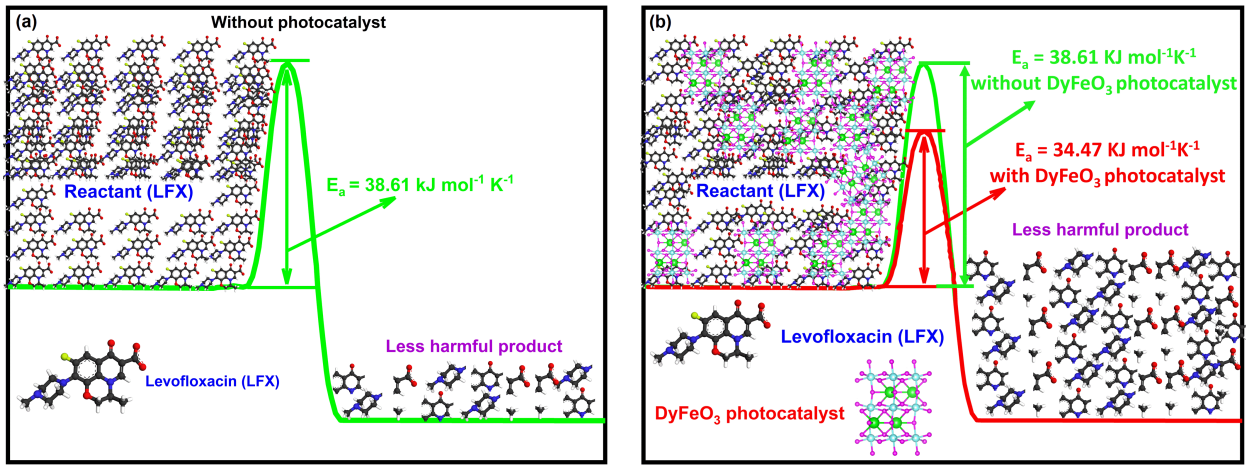

Figure 3: **Schemetic representation of the influence of activation energy in the pollutant degradation process.** The effect of activation energy on the degradation of the pharmaceutical antibiotic LFX is illustrated both in the absence **(a)** and presence **(b)** of $DyFeO_3$ nanoparticles as a photocatalyst. Notably, the $DyFeO_3$ photocatalyst effectively lowers the activation energy required for LFX degradation, leading to a substantial increase in the degradation process compared to the scenario without the photocatalyst.

Activation energy calculation

To explore the kinetics of LFX degradation, we determined the activation energy using the following Equation for LFX degradation both in the absence and presence of the $DyFeO_3$ photocatalyst, which is illustrated in Fig. 3(a,b).[51,52]

$$\ln(k) = \ln(A) - \frac{E_a}{RT} \tag{3}$$

Here, A is the pre-exponential factor, R is the molar gas constant (J mol^{-1} K^{-1}), and T is the Kelvin temperature. The value of activation energy (E_a) was calculated by the slope of $\ln(k)$ vs. $\frac{1}{T}$ graph. The corresponding graphs for this analysis are elaborated in the supple-

mentary information (Fig. S4). In the absence of $DyFeO_3$, the activation energy is higher ($38.61\,KJ\ mol^{-1}\,K^{-1}$), requiring more thermal energy for the formation of radicals and subsequent degradation of LFX. However, in the presence of $DyFeO_3$, the activation energy decreases to $34.47\,KJ\ mol^{-1}\,K^{-1}$, indicating the true catalytic role of $DyFeO_3$ nanoparticles. In essence, $DyFeO_3$ functions as a mediator for photoinduced electron transfer, thereby amplifying the generation of superoxide and hydroxyl radicals. These radicals play a crucial role in the oxidative degradation of LFX. This aligns with the principle that catalysts offer alternative reaction pathways with reduced activation energies,[53,54] facilitating a more efficient degradation of LFX through radical-mediated processes.

Apparent Quantum Yield (AQY) calculation

To quantitatively assess the photocatalyst's efficiency apart from reaction rate constants, the apparent quantum yield (AQY) was determined via the following Equation and is presented in Fig. 4(a).[50,55–57]

$$\text{Apparent Quantum Yield (AQY)} = \frac{\text{Number of degraded molecules}}{\text{Number of incident photons}} \times 100 \qquad (4)$$

The AQY values for $DyFeO_3$ in the degradation of RhB and LFX were found to be 28.94% and 32.83%, respectively, outperforming TiO_2 with an AQY of 28.6% for LFX degradation. This higher AQY in $DyFeO_3$ is attributed to its ability to minimize electron-hole recombination rates, which indicates its superior solar energy harvesting capability. In terms of practical applicability, the reusability of $DyFeO_3$ was scrutinized through four consecutive cycles of photocatalysis (Fig. 4(b)), with each cycle having a 240-minute irradiation time. Notably, the degradation efficiency remained consistently high, affirming the effective reusability of $DyFeO_3$.

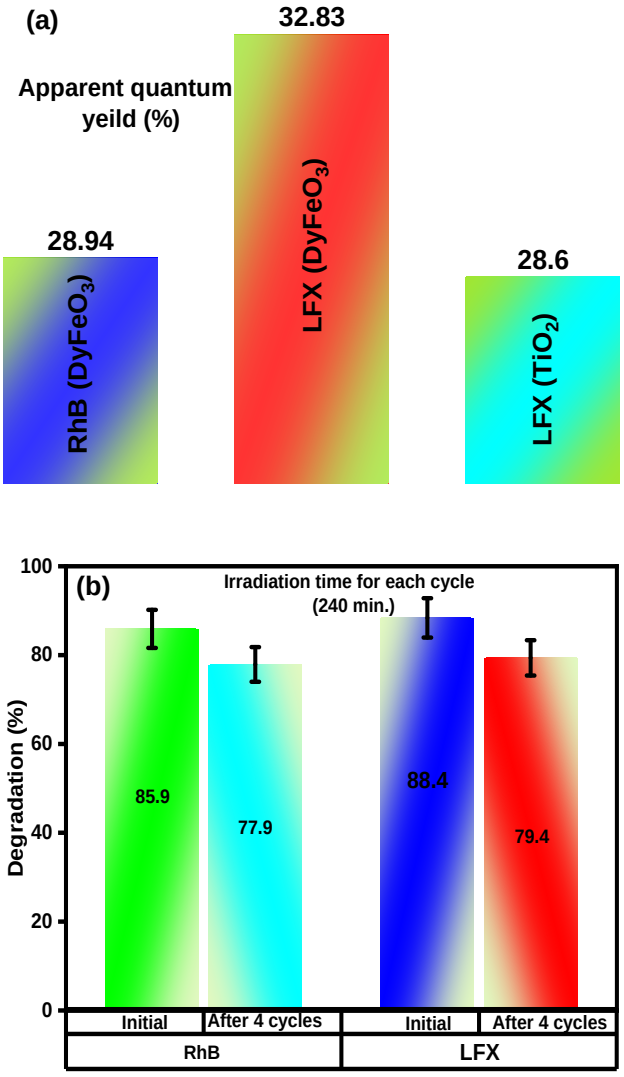

Figure 4: **Energy efficiency and reusability of $DyFeO_3$ photocatalyst. (a)** The high Apparent Quantum Yield (AQY) values established that, under similar conditions, $DyFeO_3$ nanoparticles exhibited photocatalytic activity either comparable to or surpassing that of TiO_2.**(b)** The $DyFeO_3$ photocatalyst demonstrates superior reusability, a superiors attribute with significant implications for its commercial feasibility and sustained practical application.

Active species trapping experiments

Which of the charge carriers such as the electron or hole of the $DyFeO_3$ photocatalyst is responsible for the degradation of RhB and LFX was investigated by scavenger experiments[19,47,50,55,58] including $K_2Cr_2O_7$ (e^- scavenger), EDTA 2Na (h^+ scavenger), IPA ($OH\cdot$ scavenger), and acrylamide (O_2^- scavenger) scavengers, and the results are shown in Fig. 5(a,b). The findings from the selective scavenger experiments provide valuable insights

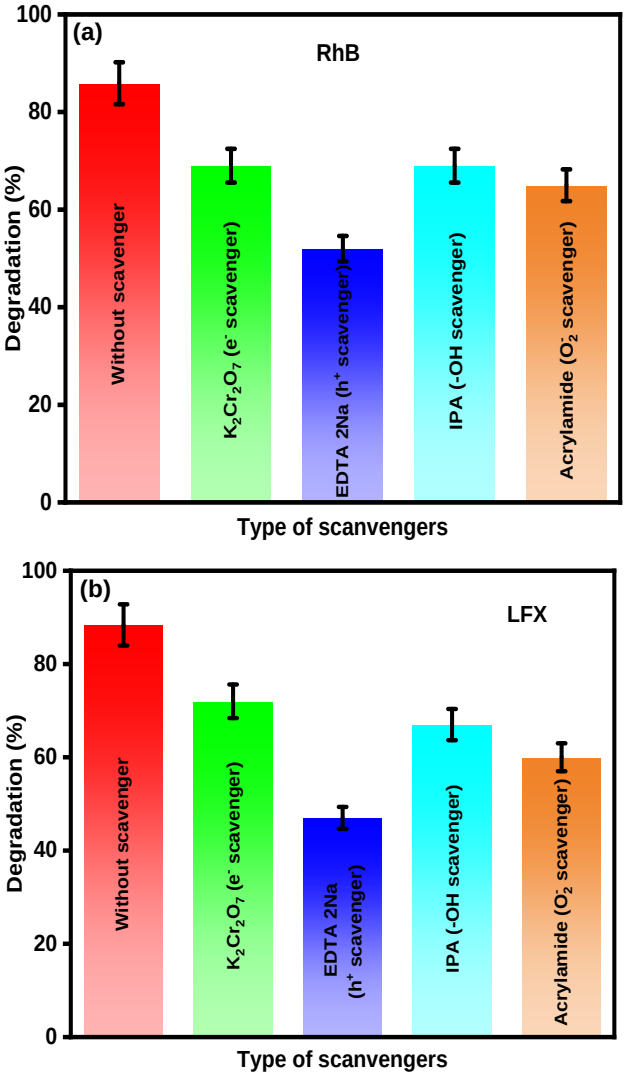

Figure 5: **Effect of reactive species on the degradation of pollutants.** The impact of various scavengers ($K_2Cr_2O_7$, EDTA, IPA, acrylamide) on the degradation process of **(a)** RhB and **(b)** LFX in the presence of $DyFeO_3$ nanoparticles was investigated, providing insights into the photocatalytic degradation mechanism, where both electrons and holes contribute, with holes being identified as the predominant reactive species governing the degradation of RhB and LFX.

into the mechanisms underlying the photocatalytic degradation of Rhodamine B (RhB) and Levofloxacin (LFX) using $DyFeO_3$ nanoparticles. In the absence of any scavenger, the degradation efficiencies of RhB and LFX are notably high, indicating the inherent photocatalytic activity of $DyFeO_3$. However, the introduction of specific scavengers targeting different charge carriers reveals distinct roles of electrons and holes in the degradation pro-

cess. Firstly, the decrease in RhB and LFX degradation in the presence of $K_2Cr_2O_7$, an electron scavenger, suggests that electrons play a crucial role in initiating the degradation reactions. This finding aligns with the proposed involvement of $DyFeO_3$ nanoparticles in reduction reactions, particularly the oxygen reduction reaction (ORR), facilitated by the elevated conduction band minimum (CBM). The scavenging of electrons by $K_2Cr_2O_7$ likely interrupts the reduction of oxygen species and subsequently reduces the efficiency of RhB and LFX degradation. Conversely, the presence of EDTA 2Na, acting as a hole scavenger, leads to a notable decrease in RhB and LFX degradation, indicating the importance of holes in oxidation reactions. The positive valence band maximum (VBM) of $DyFeO_3$ implies the existence of hole states, suggesting favorability for participating in oxidation reactions, such as the oxidation of OH^- to OH·. The scavenging of holes by EDTA 2Na likely hinders the oxidation reactions, thereby reducing the degradation efficiency of the pollutants. Additionally, the involvement of hydroxyl radicals (OH·) in the degradation process is evident from the decreased degradation efficiency of RhB and LFX in the presence of IPA, an OH· scavenger. Hydroxyl radicals are highly reactive species generated from the reaction between photogenerated holes and water molecules or hydroxide ions. The scavenging of OH· by IPA inhibits their participation in the degradation of pollutant molecules, leading to a reduction in degradation efficiency. Furthermore, the presence of acrylamide as an $O_2^-\cdot$ scavenger also results in decreased degradation efficiency of RhB and LFX, indicating the involvement of superoxide radicals ($O_2^-\cdot$) in the degradation process. Superoxide radicals can be generated through the reduction of oxygen by electrons in the conduction band of $DyFeO_3$ nanoparticles. The scavenging of $O_2^-\cdot$ by acrylamide interferes with their role in oxidizing organic pollutants, thereby reducing the efficiency of RhB and LFX degradation. Overall, the scavenger experiments collectively substantiate a comprehensive understanding of the photocatalytic degradation mechanism, where both electrons and holes contribute, with holes being the predominant reactive species in governing the degradation of RhB and LFX.

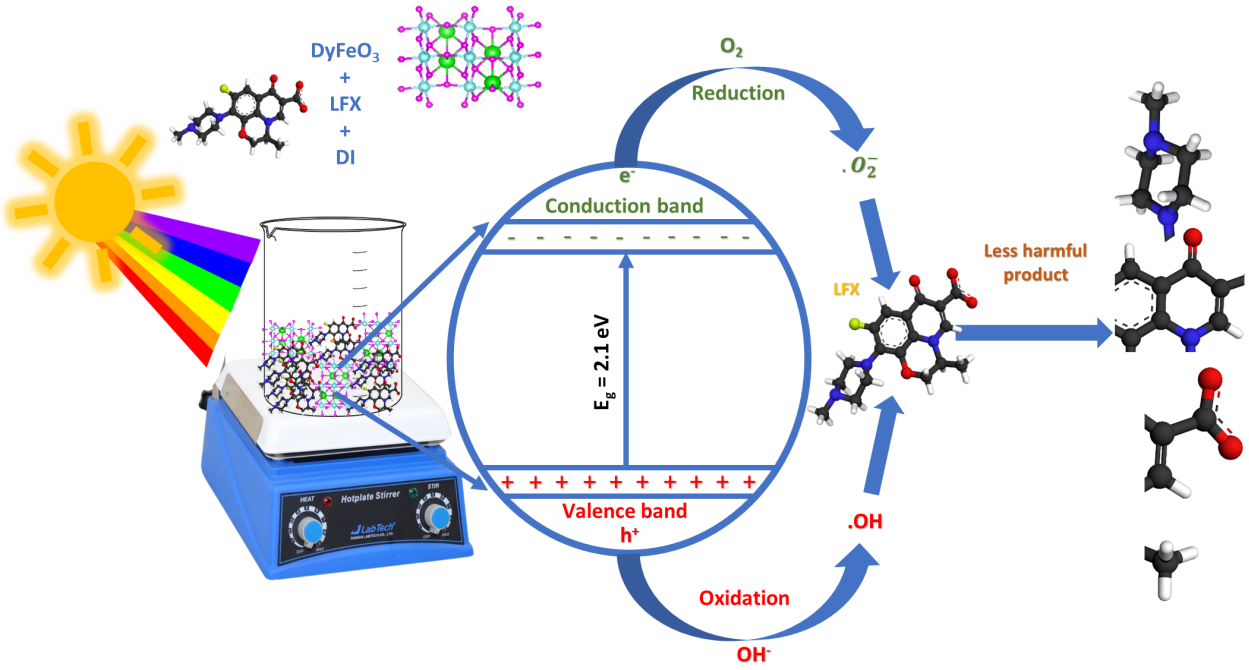

Figure 6: **Schemetic representation of the operational mechanism of photocatalysis** The proposed pollutant degradation principle by $DyFeO_3$ nanoparticles is schematically depicted. Sunlight absorption by the nanoparticles generates electron-hole pairs, initiating redox reactions with water and oxygen to yield superoxide (O_2^-) and hydroxyl (•OH) free radicals. These radicals facilitate the breakdown of organic pollutants into simpler, less harmful compounds.

Photocatalysis mechanism

Fig. 5 illustrates the schematic representation of the photocatalytic mechanism[47,59] facilitated by solar irradiation, outlining the process by which $DyFeO_3$ nanoparticles degrade Rhodamine B (RhB) and levofloxacin (LFX) in water. Upon exposure to solar radiation, $DyFeO_3$ absorbs photons with energies equal to or greater than its band gap, leading to the excitation of electrons from the valence band (VB) to the conduction band (CB). This excitation creates electron-hole pairs, where electrons are promoted to the CB while holes are left in the VB.

$$DyFeO_3 + h\nu \rightarrow DyFeO_3^*$$

$$DyFeO_3^* \rightarrow DyFeO_3 + e^- + h^+$$

Here, e^- represents the excited electron in the conduction band, and h^+ the hole in the valence band. The excited electron (e^-) and hole (h^+) are involved in redox reactions. Electrons in the conduction band can reduce molecular oxygen (O_2) to form superoxide radicals ($O_2^-\cdot$), while holes in the valence band can oxidize water (H_2O) to create hydroxyl radicals ($OH\cdot$).

$$e^- + O_2 \rightarrow O_2^-\cdot$$

$$h^+ + H_2O \rightarrow OH\cdot + H^+$$

The degradation mechanism of Rhodamine B (RhB) and levofloxacin (LFX) during photocatalysis relies on the interplay of superoxide ($O_2^-\cdot$) and hydroxyl ($OH\cdot$) radicals with the pollutant molecules. Superoxide radicals ($O_2^-\cdot$) and hydroxyl radicals ($OH\cdot$), known for their robust oxidizing properties, engage in electron transfer reactions with RhB and LFX molecules, initiating a series of molecular transformations. As photocatalysis proceeds, superoxide and hydroxyl radicals catalyze the abstraction of electrons from RhB and LFX, resulting in the formation of RhB cations (RhB^+) and LFX cations (LFX^+). These newly formed cations, inherently reactive, undergo subsequent degradation or chemical modification pathways, facilitating the conversion of RhB and LFX into smaller, less complex molecules. This stepwise degradation process ultimately leads to the efficient removal of RhB and LFX contaminants from the aqueous solution. The comprehensive breakdown of RhB and LFX demonstrates the efficacy of photocatalysis as a sustainable method for water purification, offering a promising avenue for addressing environmental pollution challenges.

$$RhB + O_2^-\cdot \rightarrow RhB^+ + O_2$$

$$RhB + OH\cdot \rightarrow RhB^+ + OH^-$$

$$\mathrm{LFX} + \mathrm{O_2^-}\cdot \rightarrow \mathrm{LFX^+} + \mathrm{O_2}$$

$$\mathrm{LFX} + \mathrm{OH}\cdot \rightarrow \mathrm{LFX^+} + \mathrm{OH^-}$$

The high degradation efficiency of $DyFeO_3$, as evidenced by the significant removal percentages of Rhodamine B (RhB) and levofloxacin (LFX), suggests that the rate of electron-hole

$$\mathrm{e^-} + h^+ \rightarrow \text{recombination}$$

recombination is low. This phenomenon can be explained by several factors inherent to the $DyFeO_3$ photocatalyst, which contribute to the effective utilization of photoinduced charge carriers. Oxygen vacancies provide favorable sites for trapping and immobilizing photoexcited electrons, preventing their rapid recombination with holes. By serving as effective charge carriers, these vacancies facilitate the separation of electrons and holes, minimizing their encounter and subsequent recombination. This enhanced charge carrier separation increases the likelihood of electrons participating in redox reactions on the material's surface, leading to improved overall photocatalytic activity. Additionally, the energy levels of the conduction band and valence band of the $DyFeO_3$ nanoparticles align favorably with the oxidation potential of hydroxyl free radical (1.8 to 2.7 V NHE) and reduction potential of superoxide free radical (-0.16 V NHE) by the following relation:

$$E_{\mathrm{CB}} - E_{\mathrm{red}} > E_{\mathrm{VB}} - E_{\mathrm{ox}}$$

This alignment promotes effective charge transfer without rapid recombination. On the other hand, the increased surface area within the porous morphology creates more active sites, allows efficient access of reactants to catalytic sites, and acts as a natural barrier for the recombination of electron-hole pairs. Furthermore, the pores serve as conduits for redox species diffusion, facilitating their movement to the surface and active participation in degradation reactions.

Post-cycle characterizations

To evaluate the structural stability of $DyFeO_3$ nanoparticles following four cycles of photocatalysis, X-ray diffraction (XRD) spectra were recorded and subjected to Rietveld refinement analysis (Fig. S5(a,b)). The XRD analysis indicates that after four cycles of photocatalysis, the degree of crystallinity of $DyFeO_3$ nanoparticles decreases, while the shape and position of the XRD peaks remain unchanged. This observation suggests that the overall structure of $DyFeO_3$is relatively stable under the photocatalytic conditions tested. However, the decrease in crystallinity could be attributed to various factors such as surface reconstruction, particle agglomeration, or the formation of defects during photocatalysis. Despite the decrease in crystallinity, the retention of peak shape and position implies that the basic crystal structure of $DyFeO_3$ is maintained, which is crucial for its photocatalytic activity.

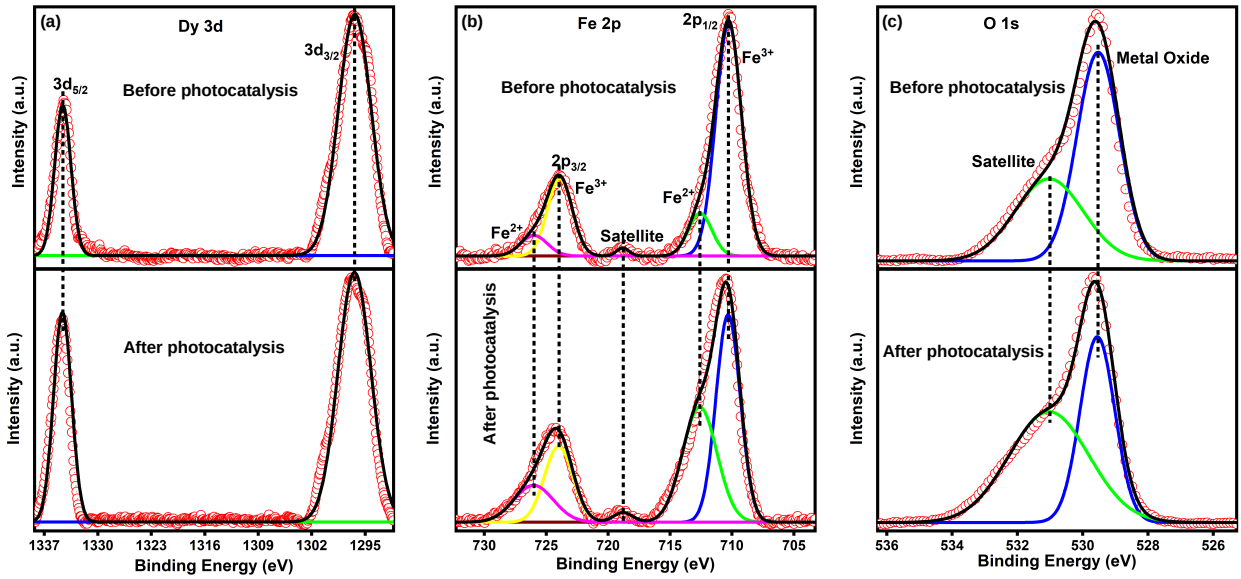

Figure 7: **Chemical state analysis of $DyFeO_3$ nanoparticles after 4 cycles photocatalysis.** High resolution XPS specta of **(a)** Dy 3d, **(b)** Fe 2p and **(c)** O 1s. XPS analysis of $DyFeO_3$ nanoparticles post-four cycles of photocatalysis reveals stable bulk composition and oxidation states of Dy, Fe, and O, while showing a notable increase in oxygen vacancies relative to metal-oxygen bonds on the surface. This suggests enhanced surface reactivity, potentially improving the photocatalyst's performance, alongside its structural robustness and chemical stability.

The stability and effectiveness of a photocatalyst rely not only on its crystallinity but also

on its surface chemistry and electronic structure, which can significantly influence its catalytic activity. Hence, an XPS analysis of $DyFeO_3$ nanoparticles post four cycles of photocatalysis was conducted, as depicted in Fig. 7, to glean insights into its surface characteristics and chemical states. The XPS analysis provides insights into the surface composition and chemical states of the elements present in the $DyFeO_3$ photocatalyst. The absence of a shift in the binding energy of various oxidation states of Dy, Fe, and O after four cycles of photocatalysis indicates that the chemical environment of these elements remains largely unchanged. This suggests that the bulk composition and oxidation states of Dy, Fe, and O within the photocatalyst are stable under the photocatalytic conditions. However, the observed changes in the O 1s XPS spectrum (Fig. 7(c)) are particularly noteworthy. Before photocatalysis, the O 1s spectrum showed peaks corresponding to metal-oxygen bonds and oxygen vacancies, with molar ratios of 61.33% and 38.67%, respectively. After four cycles of photocatalysis, these ratios shifted to 42.11% and 57.89%, respectively. This change indicates a significant increase in the proportion of oxygen vacancies relative to metal-oxygen bonds on the surface of the $DyFeO_3$ photocatalyst following photocatalysis. Oxygen vacancies are known to play a crucial role in photocatalytic processes, as they can act as active sites for adsorption and reaction of molecules involved in photocatalytic reactions.[60] The higher proportion of oxygen vacancies suggests an enhanced surface reactivity of the photocatalyst, which could potentially lead to improved photocatalytic performance.[60,61] Overall, the characterization results suggest that $DyFeO_3$ possesses promising attributes as a photocatalyst, including structural robustness, chemical stability, and surface reactivity.

Conclusions

In conclusion, our investigation into porous $DyFeO_3$ nanoparticles as a photocatalyst demonstrates their significant potential for diverse applications in environmental remediation and sustainable energy development. The porous structure and inherent oxygen vacancies of $DyFeO_3$ serve crucial roles in amplifying surface area, promoting efficient charge separation,

and thereby augmenting photocatalytic performance. Notably, the as-synthesized $DyFeO_3$ photocatalyst demonstrates noteworthy efficiency in degrading both colored and colorless probe pollutants, highlighting its versatility. Moreover, $DyFeO_3$'s presence in aqueous solutions reduces activation energy, facilitating pollutant degradation and bolstering overall reaction kinetics. These attributes feature the intrinsic photocatalytic nature of the catalyst, distinct from mere dye-sensitization effects. The observed superior degradation rates and apparent quantum yields further highlight $DyFeO_3$'s proficiency in harnessing solar energy, offering a promising avenue for addressing environmental challenges. Importantly, post-photocatalysis XPS analysis of the material reveals an enhancement in oxygen vacancies, suggesting the dynamic behavior of $DyFeO_3$ nanoparticles during catalytic processes. This increase in oxygen vacancies enhances photocatalytic efficiency by trapping electrons and mitigating recombination rates. Finally, the authentic nature, stability, and reusability of single-structured $DyFeO_3$ nanoparticles as a photocatalyst affirm their commercial viability and sustainability, positioning them as promising candidates for large-scale environmental remediation initiatives.

Acknowledgements

We sincerely acknowledge the University Grants Commission of Bangladesh for financial support, which has been instrumental in the successful execution of this research. We also acknowledge Bangladesh University of Engineering and Technology for providing essential resources crucial for conducting our experiments.

Supporting Information Available

The Supporting Information is available free of charge on the ACS Publication website at DOI: xxx.

Experimental method; UV absorption spectra of RhB and LFX; Apparent Quantum Yield (AQY) calculation; comparative photocatalytic performance of $DyFeO_3$ with other perovskite oxide; activation energy experiment; Rietveld Refinement XRD spectra of $DyFeO_3$ nanoparticle pre and post cycle photocatalysis

References

(1) Welzer, H. *Climate Wars: what people will be killed for in the 21st century*; John Wiley & Sons, 2015.

(2) Webber, M. E. *Thirst for power: Energy, water, and human survival*; Yale University Press, 2016.

(3) Loeb, S. K.; Alvarez, P. J.; Brame, J. A.; Cates, E. L.; Choi, W.; Crittenden, J.; Dionysiou, D. D.; Li, Q.; Li-Puma, G.; Quan, X.; others The technology horizon for photocatalytic water treatment: sunrise or sunset? 2018.

(4) Segneanu, A. E.; Orbeci, C.; Lazau, C.; Sfirloaga, P.; Vlazan, P.; Bandas, C.; Grozescu, I. Waste water treatment methods. *Water Treat* **2013**, 53–80.

(5) Yang, X.; Wang, D. Photocatalysis: from fundamental principles to materials and applications. *ACS Appl. Energy Mater.* **2018**, *1*, 6657–6693.

(6) Bahnemann, D. Photocatalytic water treatment: solar energy applications. *Sol. Energy* **2004**, *77*, 445–459.

(7) Kurşun, B. Energy and exergy analysis of a concentrated photovoltaic recuperator design for a geothermal based multi-generation system. *Appl. Therm. Eng.* **2020**, *181*, 115932.

(8) Melchionna, M.; Fornasiero, P. Updates on the Roadmap for Photocatalysis. *ACS Catal.* **2020**, *10*, 5493–5501.

(9) Tong, Z.; Yang, D.; Li, Z.; Nan, Y.; Ding, F.; Shen, Y.; Jiang, Z. Thylakoid-inspired multishell g-C_3N_4 nanocapsules with enhanced visible-light harvesting and electron transfer properties for high-efficiency photocatalysis. *ACS Nano* **2017**, *11*, 1103–1112.

(10) Wang, C.-C.; Li, J.-R.; Lv, X.-L.; Zhang, Y.-Q.; Guo, G. Photocatalytic organic pollutants degradation in metal–organic frameworks. *Energy Environ. Sci.* **2014**, *7*, 2831–2867.

(11) Gong, H.; Li, Z.; Chen, Z.; Liu, Q.; Song, M.; Huang, C. NiSe/$Cd_{0.5}Zn_{0.5}S$ composite nanoparticles for use in p–n heterojunction-based photocatalysts for solar energy harvesting. *ACS Appl. Nano Mater.* **2020**, *3*, 3665–3674.

(12) Bagheri, S.; TermehYousefi, A.; Do, T.-O. Photocatalytic pathway toward degradation of environmental pharmaceutical pollutants: structure, kinetics and mechanism approach. *Catal. Sci. Technol.* **2017**, *7*, 4548–4569.

(13) Guo, Q.; Zhou, C.; Ma, Z.; Yang, X. Fundamentals of TiO_2 photocatalysis: concepts, mechanisms, and challenges. *J. Adv. Mater.* **2019**, *31*, 1901997.

(14) Mclaren, A.; Valdes-Solis, T.; Li, G.; Tsang, S. C. Shape and size effects of ZnO nanocrystals on photocatalytic activity. *JACS* **2009**, *131*, 12540–12541.

(15) Khan, M. M.; Ansari, S. A.; Pradhan, D.; Ansari, M. O.; Lee, J.; Cho, M. H.; others Band gap engineered TiO_2 nanoparticles for visible light induced photoelectrochemical and photocatalytic studies. *J. Mater. Chem.* **2014**, *2*, 637–644.

(16) Rengifo-Herrera, J. A.; Pulgarin, C. Why five decades of massive research on heterogeneous photocatalysis, especially on TiO_2, has not yet driven to water disinfection and detoxification applications? Critical review of drawbacks and challenges. *J. Chem. Eng.* **2023**, 146875.

(17) Kumar, R.; Govindarajan, S.; Siri Kiran Janardhana, R. K.; Rao, T. N.; Joshi, S. V.; Anandan, S. Facile one-step route for the development of in situ cocatalyst-modified Ti^{3+} self-doped TiO_2 for improved visible-light photocatalytic activity. *ACS Appl. Mater. Interfaces* **2016**, *8*, 27642–27653.

(18) Dehghani, M.; Nadeem, H.; Singh Raghuwanshi, V.; Mahdavi, H.; Banaszak Holl, M. M.; Batchelor, W. ZnO/cellulose nanofiber composites for sustainable sunlight-driven dye degradation. *ACS Appl. Nano Mater.* **2020**, *3*, 10284–10295.

(19) Ramar, V.; Balasubramanian, K. Reduced graphene oxide/WO_3 nanorod composites for photocatalytic degradation of methylene blue under sunlight irradiation. *ACS Appl. Nano Mater.* **2021**, *4*, 5512–5521.

(20) Jung, D.; Saleh, L. M.; Berkson, Z. J.; El-Kady, M. F.; Hwang, J. Y.; Mohamed, N.; Wixtrom, A. I.; Titarenko, E.; Shao, Y.; McCarthy, K.; others A molecular cross-linking approach for hybrid metal oxides. *Nat. Mater.* **2018**, *17*, 341–348.

(21) Song, R.; Chi, H.; Ma, Q.; Li, D.; Wang, X.; Gao, W.; Wang, H.; Wang, X.; Li, Z.; Li, C. Highly efficient degradation of persistent pollutants with 3D nanocone TiO_2-based photoelectrocatalysis. *JACS* **2021**, *143*, 13664–13674.

(22) Tsang, C. H. A.; Li, K.; Zeng, Y.; Zhao, W.; Zhang, T.; Zhan, Y.; Xie, R.; Leung, D. Y.; Huang, H. Titanium oxide based photocatalytic materials development and their role of in the air pollutants degradation: Overview and forecast. *Environ. Int.* **2019**, *125*, 200–228.

(23) Choong, C. E.; Park, C. M.; Chang, Y.-Y.; Yang, J.-k.; Kim, J. R.; Oh, S.-E.; Jeon, B.-H.; Choi, E. H.; Yoon, Y.; Jang, M. Interfacial coupling perovskite $CeFeO_3$ on layered graphitic carbon nitride as a multifunctional Z-scheme photocatalyst for boosting nitrogen fixation and organic pollutants demineralization. *J. Chem. Eng.* **2022**, *427*, 131406.

(24) Preetha, R.; Govinda raj, M.; Vijayakumar, E.; Narendran, M. G.; Neppolian, B.; Bosco, A. J. Quasi-In Situ Synthesis of Oxygen Vacancy-Enriched Strontium Iron Oxide Supported on Boron-Doped Reduced Graphene Oxide to Elevate the Photocatalytic Destruction of Tetracycline. *Langmuir* **2023**, *39*, 7091–7108.

(25) Wu, J.-Y.; Chen, C.-Y.; Wang, J.; Jin, X.; Hou, W.; Kuo, H.-H.; Chiu, W.-T.; Kurioka, T.; Sone, M.; Okamoto, S.; others Tunable Photocatalytic Properties of Au-Decorated $BiFeO_3$ Nanostructures for Dye Photodegradation. *ACS Appl. Nano Mater.* **2024**,

(26) Yun, K.; Saravanakumar, K.; Jagan, G.; Yea, Y.; Yoon, Y.; Park, C. M. Fabrication of highly effective $Ag_6Si_2O_7/SmFeO_3$ heterojunction with synergistically enhanced sonophotocatalytic degradation of ciprofloxacin and production of H_2O_2: Influencing factors and degradation mechanism. *J. Chem. Eng.* **2023**, *468*, 143491.

(27) Ismael, M.; Wu, Y. A facile synthesis method for fabrication of $LaFeO_3/gC_3N_4$ nanocomposite as efficient visible-light-driven photocatalyst for photodegradation of RhB and 4-CP. *NJC* **2019**, *43*, 13783–13793.

(28) Li, X.; Shi, H.; Yan, X.; Zuo, S.; Zhang, Y.; Wang, T.; Luo, S.; Yao, C.; Ni, C. Palygorskite Immobilized Direct Z-Scheme Nitrogen-Doped Carbon Quantum dots/$PrFeO_3$ for Photo-SCR Removal of NO_x. *ACS Sustain. Chem. Eng.* **2018**, *6*, 10616–10627.

(29) Maity, R.; Dutta, A.; Halder, S.; Shannigrahi, S.; Mandal, K.; Sinha, T. Enhanced photocatalytic activity, transport properties and electronic structure of Mn doped $GdFeO_3$ synthesized using the sol–gel process. *PCCP* **2021**, *23*, 16060–16076.

(30) Kumar, A.; Kumar, A.; Krishnan, V. Perovskite oxide based materials for energy and environment-oriented photocatalysis. *ACS catal.* **2020**, *10*, 10253–10315.

(31) Afanasiev, D.; Hortensius, J.; Ivanov, B.; Sasani, A.; Bousquet, E.; Blanter, Y.;

Mikhaylovskiy, R.; Kimel, A.; Caviglia, A. Ultrafast control of magnetic interactions via light-driven phonons. *Nat. Mater.* **2021**, *20*, 607–611.

(32) Ji, Q.; Bi, L.; Zhang, J.; Cao, H.; Zhao, X. S. The role of oxygen vacancies of ABO_3 perovskite oxides in the oxygen reduction reaction. *Energy Environ. Sci.* **2020**, *13*, 1408–1428.

(33) Xiao, H.; Liu, P.; Wang, W.; Ran, R.; Zhou, W.; Shao, Z. Ruddlesden–Popper perovskite oxides for photocatalysis-based water splitting and wastewater treatment. *Energy Fuels* **2020**, *34*, 9208–9221.

(34) Barbero, N.; Vione, D. Why dyes should not be used to test the photocatalytic activity of semiconductor oxides. 2016.

(35) Tarek, M.; Yasmeen, F.; Basith, M. High Voltage Symmetric Supercapacitors Employing Porous $DyFeO_3$ Electrodes and Aqueous-Based Electrolytes. **2024**,

(36) Du, Y.; Cheng, Z.; Wang, X.; Dou, S. Lanthanum doped multiferroic $DyFeO_3$: Structural and magnetic properties. *J. Appl. Phys.* **2010**, *107*.

(37) Liu, X.; You, J.; Wang, R.; Ni, Z.; Han, F.; Jin, L.; Ye, Z.; Fang, Z.; Guo, R. Synthesis and absorption properties of hollow-spherical $Dy_2Cu_2O_5$ via a coordination compound method with $[DyCu(3,4\text{-}pdc)_2\ (OAc)(H_2O)\ _2]\bullet 10.5H_2O$ precursor. *Sci. Rep.* **2017**, *7*, 13085.

(38) Owusu, K. A.; Qu, L.; Li, J.; Wang, Z.; Zhao, K.; Yang, C.; Hercule, K. M.; Lin, C.; Shi, C.; Wei, Q.; et al. Low-crystalline iron oxide hydroxide nanoparticle anode for high-performance supercapacitors. *Nat. Commun.* **2017**, *8*, 14264.

(39) Yang, D.-Q.; Sacher, E. Characterization and oxidation of Fe nanoparticles deposited onto highly oriented pyrolytic graphite, using X-ray photoelectron spectroscopy. *J. Phys. Chem. C* **2009**, *113*, 6418–6425.

(40) Liu, R.; Wang, Z.; Peng, S.; Bi, J.; Wu, J.; Ye, Z.-G. Oxygen-vacancy-controlled magnetic properties with magnetic pole inversion in $BiFeO_3$-based multiferroics. *J. Am. Ceram. Soc.* **2020**, *103*, 1097–1104.

(41) Kistler, S. S. Coherent expanded aerogels and jellies. *Nature* **1931**, *127*, 741–741.

(42) Al-Muhtaseb, S. A.; Ritter, J. A. Preparation and properties of resorcinol–formaldehyde organic and carbon gels. *Adv. Mater.* **2003**, *15*, 101–114.

(43) Feinle, A.; Elsaesser, M. S.; Huesing, N. Sol-gel synthesis of monolithic materials with hierarchical porosity. *Chem. Soc. Rev.* **2016**, *45*, 3377–3399.

(44) Makuła, P.; Pacia, M.; Macyk, W. How to correctly determine the band gap energy of modified semiconductor photocatalysts based on UV-Vis spectra. 2018.

(45) Liu, C.; Huang, H.; Du, X.; Zhang, T.; Tian, N.; Guo, Y.; Zhang, Y. In situ co-crystallization for fabrication of g-C_3N_4/Bi_5O_7I heterojunction for enhanced visible-light photocatalysis. *J. Phys. Chem. C* **2015**, *119*, 17156–17165.

(46) Gao, E.; Wang, W.; Shang, M.; Xu, J. Synthesis and enhanced photocatalytic performance of graphene-Bi_2WO_6 composite. *PCCP* **2011**, *13*, 2887–2893.

(47) Adib, M. A.; Sharmin, F.; Basith, M. Tuning the morphology, stability and optical properties of $CsSnBr_3$ nanocrystals through bismuth doping for visible-light-driven applications. *Nanoscale Adv.* **2023**, *5*, 6194–6209.

(48) Liu, R.; Ren, J.; Zhao, D.; Ning, J.; Zhang, Z.; Wang, Y.; Zhong, Y.; Zheng, C.; Hu, Y. Band-gap engineering of porous $BiVO_4$ nanoshuttles by Fe and Mo co-doping for efficient photocatalytic water oxidation. *Inorg. Chem. Front.* **2017**, *4*, 2045–2054.

(49) Wan, C.; Zhou, L.; Sun, L.; Xu, L.; Cheng, D.-g.; Chen, F.; Zhan, X.; Yang, Y. Boosting visible-light-driven hydrogen evolution from formic acid over AgPd/2D g-C_3N_4 nanosheets Mott-Schottky photocatalyst. *J. Chem. Eng.* **2020**, *396*, 125229.

(50) Rozario, T. V.; Sharmin, F.; Shamim, S.; Basith, M. 10% La-doped $BiFeO_3$ nanoceramics: A promising magnetic catalyst to degrade pharmaceutical antibiotics. *Ceram. Int.* **2024**, *50*, 3606–3617.

(51) Hulett, J. Deviations from the Arrhenius equation. *Q. Rev. Chem. Soc.* **1964**, *18*, 227–242.

(52) Velázquez, J.; Fernández-González, R.; Díaz, L.; Melián, E. P.; Rodríguez, V.; Núñez, P. Effect of reaction temperature and sacrificial agent on the photocatalytic H_2-production of Pt-TiO_2. *J. Alloys Compd.* **2017**, *721*, 405–410.

(53) Muetterties, E. Molecular metal clusters: cluster chemistry may provide valuable insights to chemisorption and catalysis on surfaces. *Science* **1977**, *196*, 839–848.

(54) Christensen, O.; Bagger, A.; Rossmeisl, J. The Missing Link for Electrochemical CO_2 Reduction: Classification of CO vs HCOOH Selectivity via PCA, Reaction Pathways, and Coverage Analysis. *ACS Catal.* **2024**, *14*, 2151–2161.

(55) Ghosh, S.; Chakraborty, K.; Pal, T.; Ghosh, S. Photocatalytic degradation of tetracycline antibiotics by RGO-CdTe composite with enhanced apparent quantum efficiency. *Sci. Rep.* **2023**, *13*, 19028.

(56) Muñoz-Batista, M. J.; Kubacka, A.; Fernández-García, M. Effect of gC_3N_4 loading on TiO_2-based photocatalysts: UV and visible degradation of toluene. *Catal. Sci. Technol.* **2014**, *4*, 2006–2015.

(57) Barrio, J.; Mateo, D.; Albero, J.; García, H.; Shalom, M. A heterogeneous carbon nitride-nickel photocatalyst for efficient low-temperature CO_2 methanation. *Adv. Energy Mater.* **2019**, *9*, 1902738.

(58) P. P, A.; Joshi, M.; Verma, D.; Jadhav, S.; Choudhury, A. R.; Jana, D. Layered

$Cs_4CuSb_2Cl_{12}$ nanocrystals for sunlight-driven photocatalytic degradation of pollutants. *ACS Appl. Nano Mater.* **2021**, *4*, 1305–1313.

(59) Banerjee, S.; Pillai, S. C.; Falaras, P.; O'shea, K. E.; Byrne, J. A.; Dionysiou, D. D. New insights into the mechanism of visible light photocatalysis. *J. Phys. Chem. Lett.* **2014**, *5*, 2543–2554.

(60) Wang, B.; Liu, J.; Yao, S.; Liu, F.; Li, Y.; He, J.; Lin, Z.; Huang, F.; Liu, C.; Wang, M. Vacancy engineering in nanostructured semiconductors for enhancing photocatalysis. *J. Mater. Chem. A.* **2021**, *9*, 17143–17172.

(61) Tan, H.; Zhao, Z.; Zhu, W.-b.; Coker, E. N.; Li, B.; Zheng, M.; Yu, W.; Fan, H.; Sun, Z. Oxygen vacancy enhanced photocatalytic activity of pervoskite $SrTiO_3$. *ACS Appl. Mater. Interfaces* **2014**, *6*, 19184–19190.

TOC Graphic

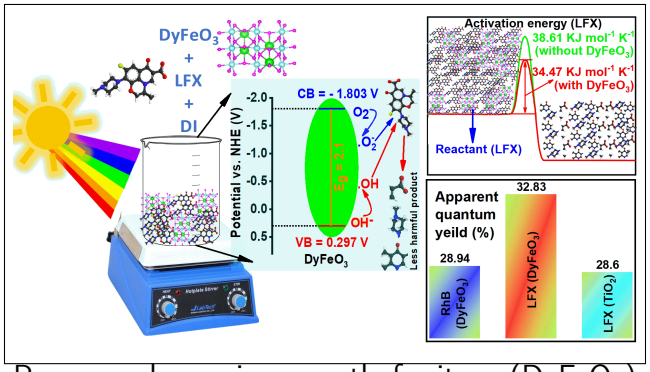

Porous dysprosium orthoferrite ($DyFeO_3$) nanoparticles exhibit promising potential in environmental remediation as a highly efficient and stable photocatalyst, boasting a direct band gap of 2.1 eV, favorable band edge positions facilitating dual involvement in reduction and oxidation reactions. Notably, $DyFeO_3$ demonstrates superior apparent quantum yield values compared to conventional photocatalysts like TiO_2, showcasing remarkable solar energy harvesting capability and catalytic efficiency, while also significantly reducing the activation energy, affirming its genuine catalytic activity in pollutant degradation processes.